npj | 2D materials and applications

www.nature.com/npj2dmaterials

ARTICLE OPEN

Check for updates

Room temperature multiferroicity in a transition metal dichalcogenide

G. Cardenas-Chirivi[1,2], K. Vega-Bustos[1], H. Rojas-Páez[1], D. Silvera-Vega[1], J. Pazos[2], O. Herrera[2], M. A. Macías[3], C. Espejo[4], W. López-Pérez[4], J. A. Galvis[5] and P. Giraldo-Gallo[1]✉

The coexistence of multiple ferroic orders, i.e., multiferroicity, is a scarce property to be found in materials. Historically, this state has been found mainly in 3-dimensional complex oxides, but so far, this state has still been elusive for the most widely studied and characterized family of 2-dimensional compounds, the transition metal dichalcogenides. In this study, we report the experimental realization of multiferroic states in this family of materials, at room temperature, in bulk single crystals of Te-doped WSe_2. We observe the coexistence of ferromagnetism and ferroelectricity, evidenced in the presence of magnetization and piezoresponse force microscopy hysteresis loops. These findings open the possibility of widening the use and study of van der Waals-based multifunctional devices for nanoelectronics and spintronics applications.

npj 2D Materials and Applications (2023)7:54 ; https://doi.org/10.1038/s41699-023-00416-x

INTRODUCTION

Multiferroics are materials that exhibit different coexisting ferroic orders, such as ferroelectricity, ferromagnetism, or ferroelasticity. Due to the coupling among the different degrees of freedom leading to these ordered states, the order parameters of one state can be controlled by tuning parameters different from their conjugate variable. For example, magnetoelectric coupling allows the control of magnetization via an electric field or, conversely, the control of electric polarization via a magnetic field for the case of ferromagnetic/ferroelectric heterostructures and multiferroics. Multiple applications in spintronics, data storage, and actuators, among others[1–4], have been envisaged and already realized. The search for new and better multiferroic materials is arduous: ferroelectrics tend to be insulators as they need to preserve electric polarization (free charges in metals screen this effect), while ferromagnets are metals in their majority[5]. In this sense, a guiding strategy that has been used to attain profitable multiferroicity is the chemical doping of either a ferroelectric host or, conversely, a ferromagnetic host. For example, the replacement of the transition-metal ion in ferroelectric $LiNbO_3$ or ZnO leads to magnetic order. On the other hand, chemical doping in complex oxides multiferroics has been effective in optimizing their properties[6,7].

Historically, these phenomena have been found mainly in 3-dimensional complex oxides and perovskites, such as Cr_2O_3, $YMnO_3$, and $BiFeO_3$, among others, or in heterostructures of ferroelectric/ferromagnetic thin films[8–10]. The 3D character of the crystal structure of these compounds poses challenges in their incorporation into nanoscale multiferroic devices. Their nanostructuration requires advanced fabrication techniques, as well as induces physical effects inherent to quantum confinement that typically weakens the multiferroic states[11]. In this sense, the use of multiferroics with an intrinsic 2D-crystalline structure is highly desirable for obtaining affordable and robust multiferroic nanodevices.

Recent advancements in the realization and study of intrinsically 2D-multiferroics have been done[12,13], for example, in the transition metal halide compounds such as NiI_2[14] and CrI_3[15,16], in the MXene $Ti_3C_2T_x$[17,18], in p-doped SnSe[19], and in doped In_2Se_3[20]. However, multiferroicity has been elusive, until now, for the most widely studied and characterized family of 2D compounds, the transition metal dichalcogenides (TMDs), in spite of numerous theoretical works in this respect[21,22]. In recent years, for this family of materials, individual ferroic orders have been experimentally observed at room temperature[23–28]. Ferromagnetism has been attained in MoS_2 and WS_2 due to defects[25,27], and in WSe_2 via chemical doping in the transition metal site[28], among other examples. Ferroelectricity has been reported in bulk-WTe_2[24], while for an odd number of layers, WSe_2 and MoS_2 are reported to be piezoelectric[29,30]. Despite the presence of these individual ferroic orders, there is no experimental evidence for simultaneous ferromagnetism and ferroelectricity in TMDs to date.

In this study, we report the experimental realization of multiferroic states in TMDs, specifically in Te-doped WSe_2. The multiferroic state is observed at room temperature and in bulk single crystals for Te doping above 7%. The multiferroic states are revealed in the observation of ferromagnetic hysteresis loops in the magnetization and ferroelectric hysteresis loops in the phase and amplitude of piezoresponse force microscopy (PFM) measurements. In addition, the highest Te-doping samples studied (15%) show very large effective piezoelectric coefficients, comparable to the commercially used 3D-piezoelectric $LiNbO_3$[31], and one order of magnitude higher than in WSe_2 and other pure TMD's nanolayers[29,30,32]. In addition, we present density functional theory (DFT) calculations which provide insights into the possible mechanisms leading to the multiferroic state. These findings open the possibility of widening the use and study of van der Waals (vdW)-based multifunctional devices and provide an affordable platform for the study of the fundamental physics of ferroic orders on low-dimensional compounds.

[1]Department of Physics, Universidad de Los Andes, Bogotá 111711, Colombia. [2]Faculty of Engineering and Basic Sciences, Universidad Central, Bogotá, Colombia. [3]Department of Chemistry, Universidad de Los Andes, Bogotá 111711, Colombia. [4]Department of Physics and Geosciences, Universidad del Norte, Barranquilla, Colombia. [5]School of Engineering, Science and Technology, Universidad del Rosario, Bogotá 111711, Colombia. ✉email: pl.giraldo@uniandes.edu.co

RESULTS

Raman spectroscopy and X-rays techniques

Figure 1a shows a picture of representative single crystals of Te-doped WSe_2, with typical lateral sizes around 1 mm and a hexagonal morphology. A level of chalcogen vacancies is naturally developed during the crystal growth process, and crystals with a general stoichiometry $W(Se_{1-x}Te_x)_{2(1-\delta)}$ are produced. x represents the fraction of Se atoms that were replaced by Te atoms, and δ is the fraction of chalcogen sites that are not occupied by either a Se or a Te. The values of x and δ for the different crystals studied were determined through X-ray fluorescence spectroscopy (see "Methods" and Supplementary Table 1 for values). Samples with four different Te-doping values, up to a maximum of $x = 15\%$, plus undoped samples ($x = 0$) with three different levels of chalcogen (Se) vacancies were characterized in this study. Two different types of X-ray diffraction measurements (powder diffraction, presented in Fig. 1d–f and Supplementary Fig. 2; and single crystal diffraction, presented in Supplementary Table 2 and crystallographic information file (CIF) (see "Data Availability" section) reveal that the crystalline structure of all the pure and Te-doped compounds is the 2H-structure (space group $P6_3/mmc$, # 194)[33]. The most intense diffraction peaks in Fig. 1d come from the {0 0 1} family of planes, given that the a-b plane of the crystals tends to align parallel to the sample holder (see "Methods"). Close inspection to the {0 0 1} diffraction peaks (Fig. 1e for the (0 0 2) peak) reveals a continuous shift to the left, and therefore, an increase of interplanar c-lattice parameter with increasing Te-doping. Single crystal diffraction confirms the increase in c-lattice parameter and, in addition, reveals an increase of the in-plane a-lattice parameter with Te-doping. Supplementary Table 2 shows a summary of a and c lattice constants found by X-ray diffraction.

The 2H-polytype is also confirmed by Raman spectroscopy. Figure 1c (see Supplementary Fig. 1 for a wider Raman shift range) shows the Raman spectra for the different Te concentrations studied ($x = 0$–15%) around the E^1_{2g} and A_{1g} modes for 2H-WSe_2. A continuous decrease in the Raman shifts of both modes as tellurium concentration increases is observed, which also reveals a 2H-structure with continuously increasing a- and c-lattice parameters. Raman peaks associated with the $1T_d$-polytype, which for pure WTe_2 appear around 150 cm^{-1} and 200 cm^{-1}, are not present, implying that secondary phase domains with this structure are not detected. Our results of the crystallographic structure align with a previous study in $W(Se_{1-x}Te_x)_2$, which reports a pure 2H-structure for Te compositions below 50%[34].

Magnetic response

Magnetization measurements as a function of magnetic field at room temperature are shown in Fig. 2a and Supplementary Fig. 3. These reveal two contributions to the magnetic signal: a diamagnetic component and a paramagnetic or ferromagnetic component, depending on the chalcogen vacancy level. The paramagnetic behavior has been previously reported by other groups in WSe_2 and other TMDs[25,26], and the paramagnetic or ferromagnetic contribution has been theoretically predicted[35] and experimentally realized in this family of materials[25–28,36–38]. Measurements of samples with different times of exposure to ambient conditions suggest that the diamagnetic component is highly dependent on the level of oxidation of the samples. For instance, freshly synthesized samples showed no or minimum diamagnetic contribution, whereas the same samples, after being stored in low vacuum for a couple of days (see "Methods"), showed a marked diamagnetic contribution (Supplementary Fig. 4). The paramagnetic/ferromagnetic contribution appears to be more robust to sample oxidation (Supplementary Figs 4 and 5, and Supplementary Table 3), and therefore the diamagnetic contribution of all curves in Fig. 2a was subtracted in order to focus on the paramagnetic/ferromagnetic component. Samples with no Te doping and low concentration of chalcogen vacancies

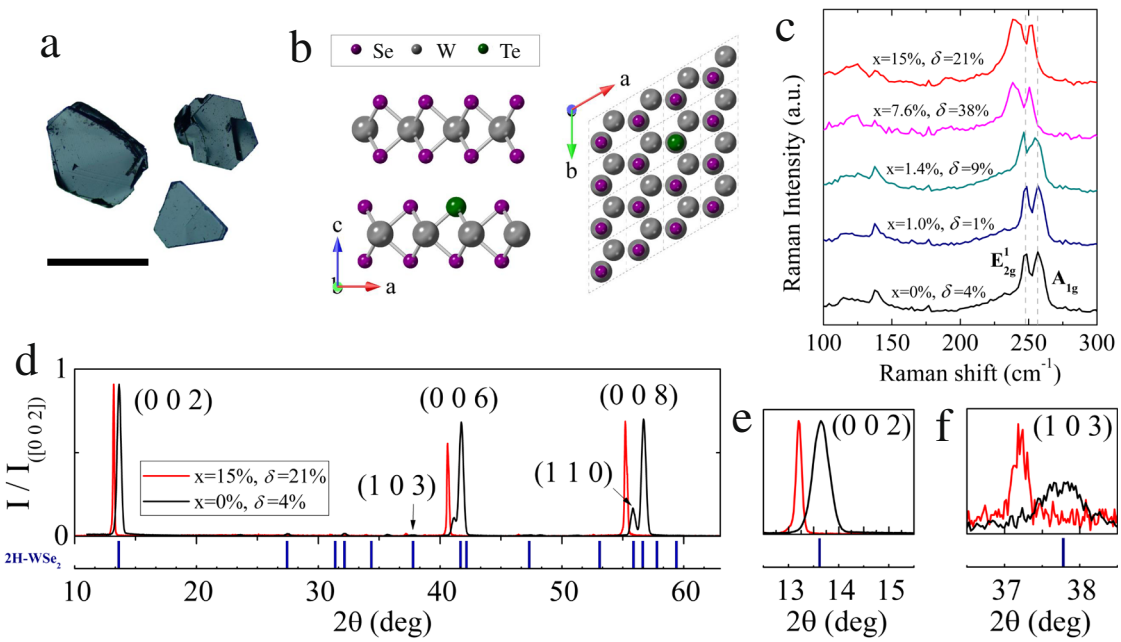

Fig. 1 Crystalline Structure. a Representative single crystals of $W(Se_{1-x}Te_x)_{2(1-\delta)}$ (this case, for $x = 15\%$ and $\delta = 21\%$) synthesized by chemical vapor transport and characterized in this work. Scale bar is 1 mm long. **b** Crystal structure of a 2H-polytype of Te-doped WSe_2 with space group $P6_3/mmc$ (# 194). **c** Raman spectroscopy measurements for $W(Se_{1-x}Te_x)_{2(1-\delta)}$ single crystals of the compositions studied in this work. Data shows a close-up look at the Raman shift around the characteristic E_{2g} and A_{1g} peaks of the 2H phase, which shift to lower values with increasing doping. Dashed gray lines indicate the peak positions for the pure $x = 0$ compound. **d** Powder X-ray diffraction data for a collection of undoped ($x = 0$, $\delta = 4\%$), and highest Te-doped ($x = 15\%$, $\delta = 21\%$) samples. Diffraction peaks are consistent with the 2H polytype, as compared with the reported peak positions of pure 2H-WSe_2, shown by the blue vertical lines[33]. **e**, **f** Close-up look to the (0 0 2) and (1 0 3) peaks, which reveal a shift to the left for the Te-doped samples, indicative of an increase of 2.5% in the c lattice parameter.

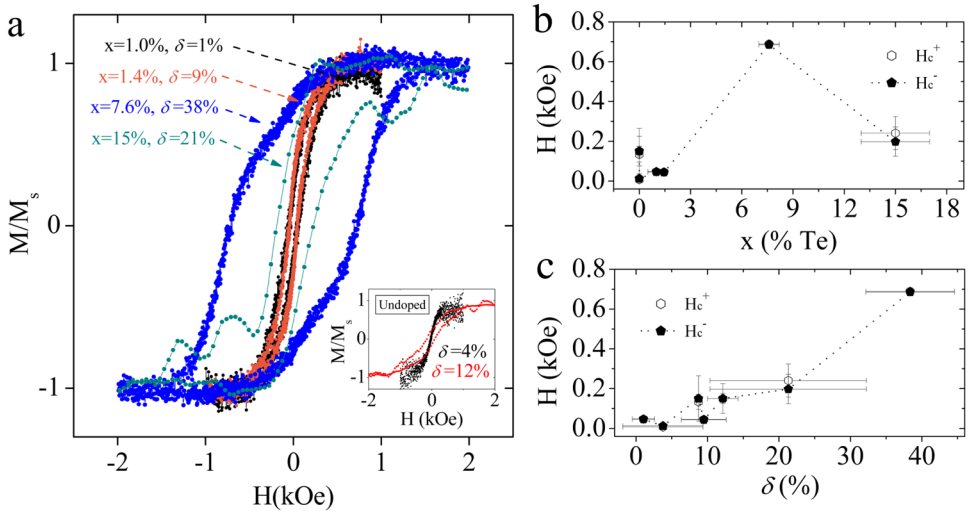

Fig. 2 Magnetic properties. a Magnetization hysteresis loops at 300 K for samples of $W(Se_{1-x}Te_x)_{2(1-\delta)}$ with different x and δ values. For all curves, the diamagnetic components were subtracted, and their values were normalized by the saturation magnetization, M_s. Inset in (**a**) shows the hysteresis loops for undoped ($x = 0$) $WSe_{2(1-\delta)}$ samples with different amounts of chalcogen vacancies, δ. **b** and **c** show coercive fields H_c for all samples presented in (**a**), as a function of **b** Te-doping, x, and **c** chalcogen vacancies, δ. Vertical error bars are obtained as the maximum H_c dispersion around the $M = 0$ axis, and horizontal error bars are calculated through the standard deviation of the composition data.

(black curve in the inset to Fig. 2a) show a paramagnetic behavior, with a saturating magnetization above fields of the order of 150 Oe. Te-free samples with an increased number of Se vacancies showed weak hysteresis loops with small coercive fields, indicating weak ferromagnetism (see red curve in the inset to Fig. 2a and Supplementary Fig. 4a–c for other vacancy levels). For all the Te-doped samples studied, the ferromagnetic hysteresis loops became more notorious, reaching a maximum coercive field of 700 Oe for the sample with $x = 7.6\%$ and $\delta = 38\%$. Figure 2b, c plots the coercive field for the different samples studied as a function of Te doping (x) and chalcogen vacancies (δ), respectively. The coercive field as a function of chalcogen vacancies grows monotonically, in contrast to its behavior as a function of Te doping. This suggests that magnetism is driven by the amount of chalcogen vacancies. Nevertheless, the apparent strengthening of the ferromagnetism in the Te-doped samples, in contrast to the undoped samples, suggests some role of the Te atoms. We argue that this is due to the fact that the presence of Te in the synthesis promotes the formation of chalcogen vacancies, as supported by the data in Supplementary Table 1. For instance, all the Te-free syntheses reached maximum vacancy levels of 12%, even though for some of them, nominal vacancy values of 50% were aimed. Whereas for the Te-doped synthesis, measured vacancy levels above 12% could be easily reached, with a maximum obtained vacancy level of 38%. Other works in transition metal ditellurides have reported challenges to attain perfect stoichiometries and a tendency to the formation of a large number of chalcogen vacancies when compared to diselenides or disulfides[39,40]. Moreover, previous works in transition metal ditelluride alloys have reported a decrease in the chalcogen vacancies energy formation as going from a 2H to a 1 T_d crystal structure[41,42], which is realized in $W(Se_{1-x}Te_x)_2$ for values of $x > 0.5$[34,43]. Therefore, a tendency for a larger number of chalcogen vacancies is expected in our samples as Te doping increases, consistent with the data presented in Supplementary Table 1.

Piezo- and ferroelectric response

Piezoelectricity in these compounds was investigated using an atomic force microscope (AFM) through the Dual AC Resonance Tracking (DART) piezo force microscopy (PFM) technique (see "Methods"). Freshly cleaved samples were measured in an inert N_2 atmosphere in order to prevent surface oxidation and minimize electrostatic effects. This technique measures the amplitude of elongation for a given applied AC bias, and therefore it is a direct measurement of the piezoelectric response. Figure 3a–c shows DART piezoresponse maps for different values of the AC bias voltage in single crystals with three different doping levels. The color in each plot represents the amplitude of out-of-plane deformation, which spatial average increases with the AC applied bias. The spatially averaged piezoresponse as a function of AC bias, presented in Fig. 3d, is linear for all samples. The slope in each curve is equivalent to the effective piezoelectric constant d_{33} (see "Methods"). The two lowest Te-concentration samples exhibit comparable values for their effective d_{33}, of the order of 4 pm V^−1. This value is similar to the piezoelectric constants previously reported for TMD monolayers[30,44] and higher than the d_{11} coefficient reported for a WSe_2 monolayer[29,32]. For the highest Te-doped sample, with $x = 15\%$ and $\delta = 21\%$, $d_{33} = 26 \pm 4$ pm V^−1. This remarkably high value is comparable to the d_{33} of PPLN—a device based on $LiNbO_3$, a widely used piezoelectric material[31]—and it is the highest reported or predicted d_{33} value among the TMDs in any configuration[45,46]. It is important to mention that previously reported piezoelectric properties in the TMDs have been measured in nanostructures of these compounds, generally in single layers in which centrosymmetry is broken, and recently, in thin films of TMD alloys[47]. Our measurements are performed in macroscopic bulk single crystals. The high piezoelectric coefficients found in our work are comparable to the coefficients of materials used in commercial piezoelectric devices.

In order to further characterize the electromechanical properties in these compounds, switching spectroscopy (SS)-PFM measurements were performed (see "Methods" for experimental details). The phase (Fig. 3e, g, i) and amplitude (Fig. 3f, h, j) of the SS-PFM piezoresponse were recorded as a function of the DC bias voltage at different random locations over the samples (insets to Fig. 3e, g, i). The $x = 1.4\%$, $\delta = 9\%$ Te-doped crystal (Fig. 3e, f) reveals a piezoelectric response without hysteresis. Interestingly, the amplitude tends to saturate for $|V_{DC}| > 1$ V, suggesting a possible saturation of the electric dipole moment response. The $x = 7.6\%$, $\delta = 38\%$ and $x = 15\%$, $\delta = 21\%$ Te-doped samples show clear hysteresis loops both in the amplitude and phase of the SS-PFM piezo-response (Fig. 3g, h and 3i, j, respectively), with shapes equivalent to the ones shown in prototypical ferroelectric

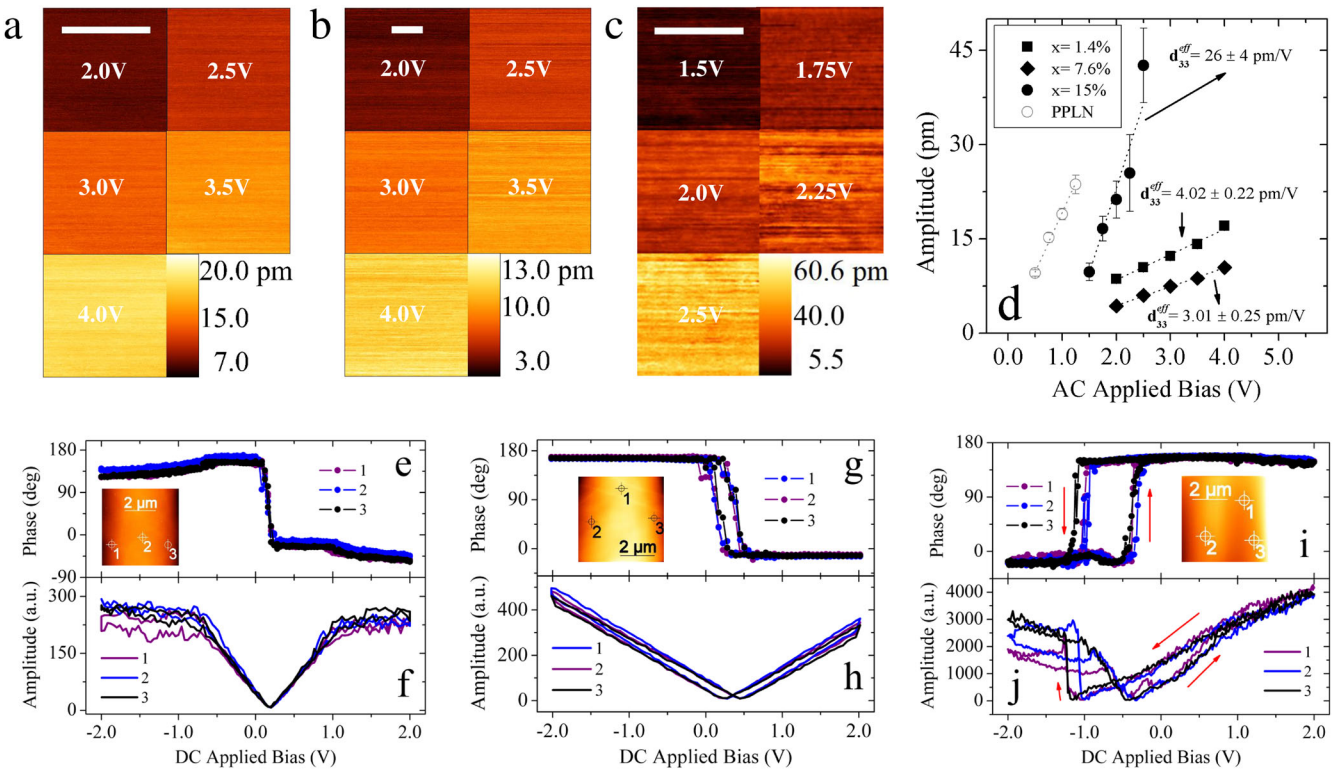

Fig. 3 Ferroelectric properties. DART-PFM piezoresponse amplitude normalized by SHO model as a function of the AC applied bias for $W(Se_{1-x}Te_x)_{2(1-\delta)}$ samples with **a** $x = 1.4\%$, $\delta = 9\%$; **b** $x = 7.6\%$, $\delta = 38\%$; and **c** $x = 15\%$, $\delta = 21\%$. Scale bars of all three figures are 200 nm long. **d** Spatial average of the DART-PFM piezoresponse values from (**a**), (**b**) and (**c**) versus AC applied bias. The effective d_{33} piezoelectric coefficient is obtained from the slope of these curves. The curve for a sample of PPLN is included for comparison purposes. Error bar for each point represents the standard deviation of the amplitude within each image for each voltage. SS-PFM piezoresponse phase and amplitude for samples with **e**, **f** $x = 1.4\%$, $\delta = 9\%$; **g**, **h** $x = 7.6\%$, $\delta = 38\%$; and **i**, **j** $x = 15\%$, $\delta = 21\%$. Insets to all phase curves show topography images indicating the exact locations at which the SS-PFM piezoresponse curves were performed.

materials such as $BaTiO_3$ and PZT[48]. These loops indicate the presence of domains of electric polarization that can be aligned, with a coercive voltage of 0.2 V and 0.5 V for the $x = 7.6\%$ and 15% Te-doped bulk samples, respectively, and therefore reveal that these materials are ferroelectric. Provided that all ferroelectrics are piezoelectrics[49,50], both properties in this material should originate from the same mechanisms.

In addition, electrical current vs voltage (IV) measurements taken in the Te-doped samples reveal asymmetric and hysteretic curves (Supplementary Fig. 10) with similar characteristics to those measured in the prototypical ferroelectric $BaTiO_3$ and multiferroics such as $BiFeO_3$[51]. This makes Te-doped WSe_2 suitable for a variety of multifunctional applications in electronic devices[52].

As presented before, the crystalline structure of our samples is the centrosymmetric 2H polytype. Previous reports of piezoelectric behavior in monolayer TMDs, and ferroelectric behavior in WTe_2 have attributed the non-centrosymmetric structures in those systems as the underlying mechanism for the existence of electric dipole moments. Therefore, these results invite us to search for alternative mechanisms for ferroelectricity in the TMDs, as will be presented in the "Computational modeling" and "Discussion" sections.

Computational modeling results

In order to gain further insight into the mechanisms that can lead to the multiferroic properties of $W(Se_{1-x}Te_x)_{2(1-\delta)}$, first-principles calculations were performed using density functional theory (DFT) (see "Methods"). For each concentration, random configurations were selected to perform the calculations. The resulting total magnetizations for different levels of Te doping and chalcogen vacancies can be found in Supplementary Table 4 for one particular realization of each composition. Interestingly, the system with the highest magnetic moment corresponds to the one with the highest value of chalcogen vacancies, δ, independent of the value of Te doping, x.

Figure 4 shows different views of two layers of a simulated crystal structure with $x \simeq 10.26\%$ and $\delta \simeq 39\%$, very close to the values of one of our experimentally characterized samples that show the strongest ferromagnetism and intermediate ferroelectricity. Arrows in Fig. 4c represent the magnetic moment contribution per atom for the atoms that contribute the most magnetic moment in this configuration. In this figure, in order to facilitate visualization, bonds between W atoms are drawn if the interatomic distance is equal or less than the bond distance in crystalline tungsten (2.74 Å); and bonds between W and chalcogen atoms are drawn if the interatomic distance is less than 2.72 Å and 2.747 Å for W-Se and W-Te bonds, respectively. The W atoms that are not bonded to a chalcogen element in the figure (labeled as W24 in Fig. 4a and W1 and W5 in Fig. 4b) are the ones that contribute the most magnetization of all atoms in the structure (as represented by the length of the gray arrows in Fig. 4c). The next-higher contributions come from W atoms that have a reduced number of bonds with chalcogen atoms (this is, W atoms labeled as 17, 21, 23, 25, 28 and 29 in Fig. 4a, and 4, 6 and 16 in Fig. 4b, displayed as red arrows in Fig. 4c). The magnitude of the contributions seems to be unaffected by whether the W is bonded to Te or Se atoms. Therefore, the relevant parameter that drives the magnitude of the magnetic moment is the number of bonds of each W with neighboring chalcogen atoms. Although the criteria for drawing a bond in Fig. 4 is rather arbitrary, a different number of bonds for each W ion is an indication of a

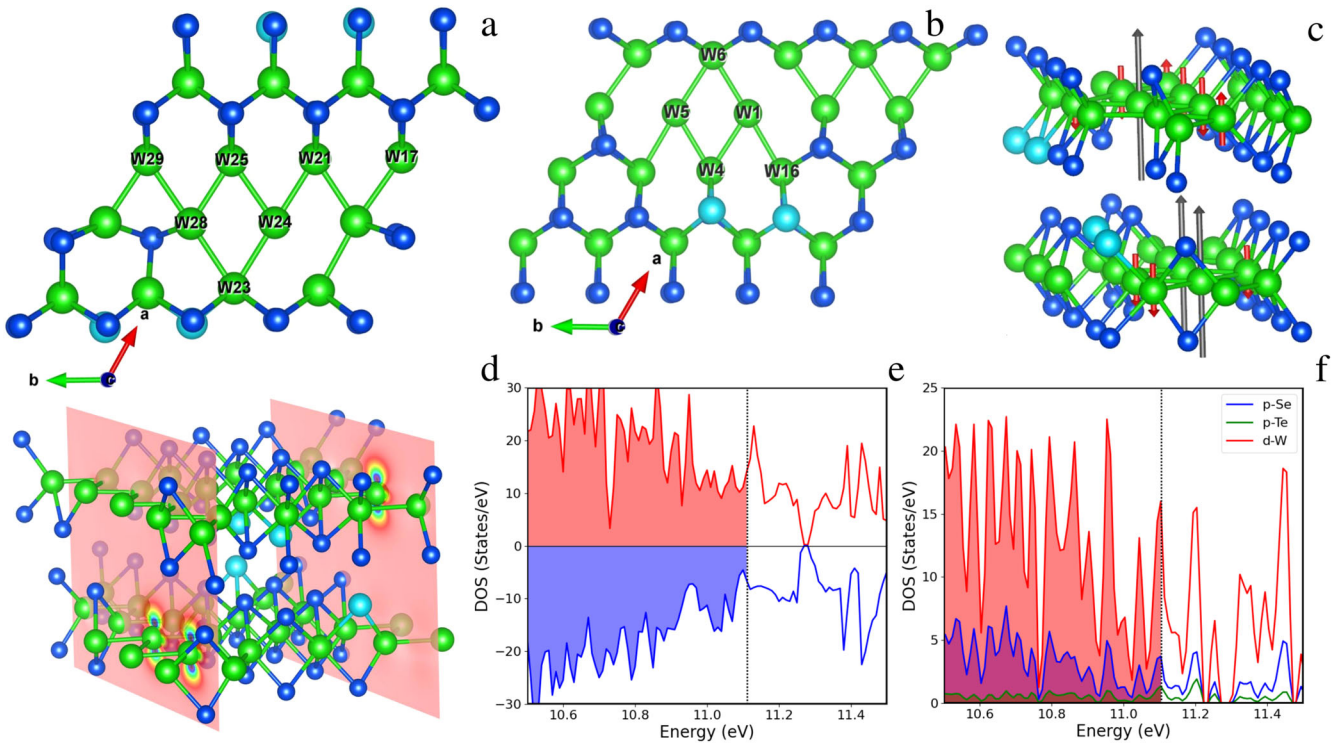

Fig. 4 Modeling of structural and magnetic properties. Structural and magnetic calculations of $W(Se_{1-x}Te_x)_{2(1-\delta)}$ for $x = 10.26\%$ and $\delta = 39.06\%$. W-W and W-Te bonds are drawn if the interatomic distances are less than 2.74 Å and 2.81 Å, respectively (see text). Top views of the **a** superior and **b** inferior monolayers and **c** perspective view of the optimized structure. Arrows indicate resulting atomic magnetic moments more than 0.02 μ_B in magnitude. **d** Spin density plotted on planes containing atoms W1, W5 and W24. To facilitate visualization, atom W24 from a neighboring unit cell is depicted. **e** Total spin-up (red) and spin-down (blue) density of states. **f** Projected density of states on p orbitals of Se and Te atoms and on d-orbitals of W.

different local environment for each. Therefore, our calculations indicate that the magnitude of the W magnetic moment in this system is driven by the local environment of the W atoms and the strength of its hybridization to chalcogen atoms (or, alternatively, its bonding to a chalcogen vacancy). Figure 4d shows the local spin density, $n_s(\mathbf{r}) = n_u(\mathbf{r}) - n_d(\mathbf{r})$, where n_u (n_d) is the density of spin-up (spin-down) electrons, plotted on two planes containing W1, W5 and W24 (atoms without bonds to chalcogen atoms). It is important to notice that throughout the unit cell, the spin density keeps low values of $\sim\pm5\times10^{-4}$ μ_B (pink), while on these three atoms, the spin density peaks at $\sim8.8\times10^{-2}$ μ_B (violet). For the atoms not bonded to a chalcogen element in Fig. 4a–c, atomic magnetization (the integral of the spin density up to the covalent radius) takes values as high as 0.56 μ_B. Furthermore, the overall ferromagnetic character of the system is corroborated by means of the total density of states (DOS) for spin-up and -down (Fig. 4e), which shows that at the Fermi energy, there is a larger contribution from the spin-up channel (red) than from the spin-down channel (blue). The projection of the DOS on atomic orbitals allows for the identification of tungsten d-orbitals as the electronic states associated with the found magnetic order, as shown in Fig. 4f and Supplementary Fig. 11a.

In order to corroborate if magnetic order is dependent on the positions of chalcogen vacancies and/or Te substitutions, calculations were performed for a different configuration keeping the same concentration of vacancies and Te doping. In this second configuration (Supplementary Fig. 11b), there is a more homogeneous distribution of vacancies which causes all W-atoms to be bonded to at least one chalcogen atom, either Se or Te. The resulting supercell magnetization is null in this case, with almost negligible atomic magnetizations (around 10^{-4} μ_B) with opposite directions uniformly distributed throughout the cell.

In order to find possible sources for the ferroelectric state, electric polarization and ferroelectric behavior were analyzed in the framework of the modern theory of polarization[53], which allows to obtain the unit-cell polarization from the Berry phase of the system. The electric polarization vector was calculated in the same systems for which magnetization was studied. Results show a dependency on vacancy concentration and Te doping, as can be seen in Supplementary Table 5. Additionally, Hirshfeld charge analysis[54] was carried out in order to identify both the atoms responsible for polarization and the possible mechanism of ferroelectricity.

In the case of pristine WSe_2, it is found that chalcogen atoms have positive Hirshfeld charges while W atoms gain a negative charge which is approximately equal to twice the charge of the chalcogens. This is expected from the coordination numbers of Se and W, three and six, respectively (Supplementary Table 5). This distribution of charge makes each layer of 2H-WSe_2 non-polar due to its centrosymmetry, which is broken by the presence of vacancies. As can be seen in Fig. 5, for the same simulated atomic configuration and concentrations as the one in Fig. 4 ($x \simeq 10.26\%$ and $\delta \simeq 39\%$), the absence of a Se atom develops electric polarization directed from the negative W plane toward the remaining Se atom below or above the vacancy. Since the sign of the polarization depends on the position of the chalcogen atom, this result suggests that polarization could be reverted by moving the chalcogen atom (or equivalently, the chalcogen vacancy) from one face of a layer to the other face, passing through the triangular space defined by the neighboring W atoms. This establishes the intralayer motion of a chalcogen vacancy as a possible mechanism for the presence of switchable electric dipole moments in WSe_2. Interestingly, even though for this configuration there is a high concentration of vacancies ($\delta \simeq 39\%$), there is only one place with a non-mirrored vacancy located at the top

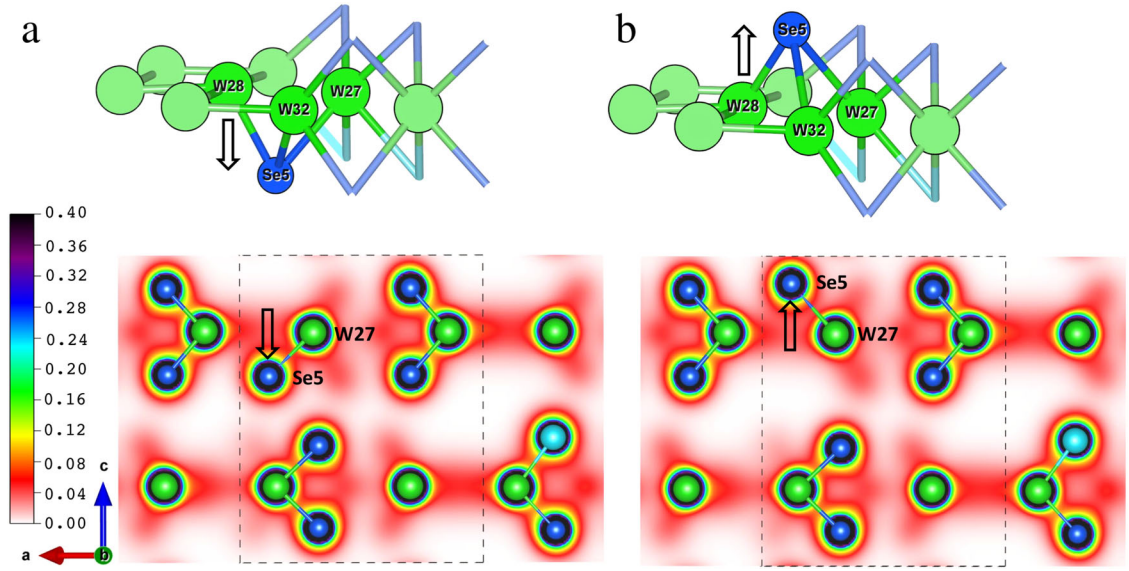

Fig. 5 Ferroelectric switching model. Electric polarization calculations of $W(Se_{1-x}Te_x)_{2(1-\delta)}$ for $x = 10.26\%$ and $\delta = 39.06\%$. **a** Different views of a (0 1 0) plane of a $W(Se_{1-x}Te_x)_{2(1-\delta)}$ for the same atomic configuration as in Fig. 4. The top view is a 3D-perspective image of the atoms around a chalcogen vacancy located in the upper side of the top layer of the unit cell. The bottom view shows both layers of the unit cell (marked in the dashed square), and the color scale represents a slice of the total electronic density (color bar scale in a.u.). Arrows indicate the direction of the electric dipole moment around the vacancy in the *c*-direction. **b** Same representations as in (**a**), but now with the chalcogen vacancy located in the bottom side of the top layer of the unit cell. The direction of the electric dipole moment is flipped in this case, as indicated by the arrow.

layer. The remaining vacancy sites are located on both sides of both layers of the unit cell, therefore not breaking its centrosymmetry, as can be seen in the bottom layers of the unit cell in Fig. 5. For some configurations, the resulting perpendicular polarization (6.04 μC/cm^2) is one order of magnitude larger than the reported values for other 2D materials[55].

An alternative mechanism is the interlayer vacancy diffusion[56], where a vacancy from the top face of a layer migrates to the bottom face of the layer just above it, or vice versa. Considering both the Hirshfeld charges of chalcogen atoms and the sign of the polarization obtained from the Berry phase, it can be seen that interlayer vacancy diffusion also triggers electric polarization switching. In this case, the dipole moment is transferred from one layer to the other as opposed to the intralayer mechanism for which the polarization remains in the same layer.

In order to evaluate the activation barrier associated with the ferroelectric switching mechanisms just described, nudged elastic band (NEB)[57] calculations were performed in a simplified 2×2×1 supercell with just one Se vacancy. The resulting activation energy curves are found in Supplementary Fig. 13a, b. Although the energy barriers are high (4.1 eV for intralayer and 3.67 eV for interlayer), possibly due to the large rigidity of the one-vacancy supercell, these calculations show that both mechanisms are comparable energetically. A reduction of the energy barriers can be expected in simulation supercells with vacancies and Te doping closer to the real samples (see "Methods"). Sliding ferroelectricity[58] has not been considered, given both the 2H symmetry of the samples and the random nature of the vacancies' location. However, it could be possible that certain configurations of the vacancies lead to this type of ferroelectric switching. Determination of the mechanisms responsible for the large piezoelectric response and ferroelectricity in Te-doped WSe_2 remains an open research subject.

To study the effect of Te doping on the electric polarization, Se5 (as labeled in Fig. 5) was exchanged by a Te atom. The resulting Hirshfeld charge of this Te is ~2.61 times larger than that of Se5, and the total polarization of the supercell presents a ~20 times enhancement if compared to the previous system. The larger separation of charge seen with Te can be ascribed to the difference in its electronegativity (χ) with respect to both Tungsten and Selenium. In Pauling units $\chi^{Se} = 2.55$, $\chi^{W} = 2.36$ and $\chi^{Te} = 2.1$, which accounts for the larger migration of charge from Te to W atoms. An additional configuration with a higher concentration of Te and fewer vacancies was studied ($x = 16\%$ and $\delta = 21.88\%$). In this case, there are 13 non-mirrored vacancies, and chalcogen atoms are distributed on both faces of the two layers of the unit cell, 9 on the superior face and 4 on the inferior face. In general, Hirshfeld charges of Te range from 2 to 3 times the charges of Se, which gives larger local electric dipole moments. Since several local dipoles have opposite directions depending on the position of the vacancies, the computed unit cell polarization is about the same value found for the configuration with only one non-mirrored vacancy. In the case where all local dipoles point in the same direction, a large unit-cell polarization is expected.

DISCUSSION

Ferromagnetic states have been predicted theoretically[35] and experimentally realized in TMD through defects formation[25], vacancies formation[27], proton irradiation[37], nanostructuration[38], and doping with magnetic impurities[26,28]. In the case of this study, the dependency of the coercive fields on Te doping and chalcogen vacancies suggests that the magnetic properties of bulk $W(Se_{1-x}Te_x)_{2(1-\delta)}$, are driven by the number of chalcogen vacancies, rather than by the presence of Te. This result aligns with the mechanism for ferromagnetic order derived from our DFT calculations, which reveals that the spin density is strongly localized onto the d-orbitals of the W-atoms less bonded with chalcogen atoms (or equivalently, more bonded to chalcogen vacancies), as presented in Fig. 4f and Supplementary Fig. 11. This suggests that unpaired/localized d-electrons in W are responsible for the observed magnetic behavior. The key role of chalcogen vacancies in the magnetic order of TMDs has been previously predicted and experimentally observed in systems such as MoS_2[59], WS_2[27] and monolayer V-doped WSe_2[36]. For instance, the presence of vacancies in 2H-MoS_2 nanosheets has been shown to transform

the crystalline structure around the vacancies into a 1T-structure[59]. In this environment, the Mo^{4+} ions have a net magnetic moment, in contrast to stoichiometric 2H-MoS_2, in which the Mo^{4+} ions are non-magnetic. Data suggest that the origin of the measured ferromagnetism in this system is intimately connected to an enhanced Mo^{4+}-S-vacancy exchange interaction. Similar conclusions have been recently reached in monolayer V-doped WSe_2, in which ferromagnetic properties are significantly enhanced by promoting Se vacancies in the structure[36]. In the case of $W(Se_{1-x}Te_x)_{2(1-\delta)}$, the role of chalcogen vacancies can be completely analogous to their TMD counterparts. This is, a local magnetic moment is generated in the d-orbitals of transition metal atoms surrounded by vacancies due to their modified local environment. This can result in a strengthening of the exchange interaction through their coupling with chalcogen vacancies, leading to the ferromagnetic state.

On the other hand, ferroelectric states have been commonly associated with the non-centrosymmetry inherent to certain crystal structures. Among the TMDs, piezoelectric and ferroelectric properties have been previously reported in crystals with the non-centrosymmetric $1T_d$-phase, like the case of pure WTe_2[24], or in nanostructures of the 2H-polytype with an odd number of layers, for which centrosymmetry is broken[29,30]. However, alternative mechanisms, other than the underlying bulk crystalline symmetry, have been proposed for the appearance of electric polarizations in ferroelectric materials. For example, in type-II multiferroics such as $TbMnO_3$[60], Ca_3CoMnO[61] and the 2D material NiI_2[14], local electric polarization is proposed to be induced by the strong spin-orbit coupling in a magnetic host, which can lead to inversion symmetry breaking, and to a ferroelectric state. In addition, and for the specific case of TMDs, inequivalent Te-W distances in adjacent WTe_2 layers have been theoretically shown to induce a charge imbalance, leading to an out-of-plane electric polarization[62]. In the case of this work, our DFT calculations identify a feasible mechanism for the existence of electric dipole moments in the 2H unit cell that can lead to a non-zero total electric dipole moment in the crystal. In our model, the electric dipoles are originated in the charge imbalance created by a chalcogen vacancy aligned with a chalcogen atom in the *c*-direction. Our calculations indicate that such imbalance is an order of magnitude stronger if the chalcogen is a Te atom, which is consistent with our experimental results: no ferroelectric state is found in the pure $WSe_{2(1-\delta)}$, in which, although the charge imbalance mechanism due to vacancies is also present, it is possibly not strong enough to result in a ferroelectric state. Whereas ferroelectricity grows stronger with Te doping, being well established for the largest Te-doped crystals.

For $W(Se_{1-x}Te_x)_{2(1-\delta)}$, the role of chalcogen vacancies seems to be crucial for both ferromagnetic and ferroelectric states. Interestingly, each of these ferroic orders in this material can exist independently from the other: $WSe_{2(1-\delta)}$ is only ferromagnetic, and WTe_2 is only ferroelectric. This, together with the fact that multiferroicity in $W(Se_{1-x}Te_x)_{2(1-\delta)}$ is observed at room temperature, suggests that, although part of the origin of both ferroic orders can be common, this material is not a type-II multiferroic. In this class of multiferroics, the mechanisms for both ferroic orders are highly intertwined through spin-orbit coupling and generally show cryogenic critical temperatures[60]. Nevertheless, the strong influence of chalcogen vacancies on both ferroic orders in $W(Se_{1-x}Te_x)_{2(1-\delta)}$ makes possible not only the simultaneous presence of these states but also their magnetoelectric coupling—a crucial ingredient in several envisaged applications of multiferroic materials. These ingredients, combined in an intrinsically 2D vdW layered material and at room temperature, open the door to a wide use of nanostructured multiferroic devices.

METHODS

Synthesis of single crystals

Tellurium-doped tungsten diselenide single crystals, $W(Se_{1-x}Te_x)_{2(1-\delta)}$ (with $x = 0$–15% and $\delta = 1$–38%), were grown by chemical vapor transport (CVT) with iodine as transporting agent. Powders with the desired stoichiometry were produced from elemental W, Se and Te through a sintering process. For each batch, stoichiometric amounts of tungsten (No. 357421, Sigma Aldrich), selenium (No. 36208, Alfa Aesar) and tellurium (No. 266418, Sigma Aldrich) were thoroughly ground and then cold-pressed at 1000 psi to form a pellet. The pellet was sealed in a quartz tube, leaving a small pressure of argon inside the quartz ampoule. The ampoule was then heated from room temperature to 500 °C for 24 h and maintained at this temperature for 72 h. The obtained sintered powder and the iodine were then encapsulated in vacuum in a long quartz tube and then placed in a two-zone tube furnace with 1010 °C in the hot zone and 900 °C in the cold growth zone for 144 h. The single crystals were collected from the growth zone of the tubes. The obtained crystals were stored in a vacuum desiccator which reaches absolute pressures of ~300 Torr and relative humidity of 30%. This delays but does not prevent sample oxidation and degradation.

X-ray diffraction

The doping values x and δ of our $W(Se_{1-x}Te_x)_{2(1-\delta)}$ single crystals were determined by triplication in X-ray fluorescence (XRF) using a ZSX Primus RIGAKU spectrometer.

X-ray powder diffraction patterns of $W(Se_{1-x}Te_x)_{2(1-\delta)}$ single crystals for all compositions were obtained using an Empyrean PANalytical series 2 diffractometer with a CuKα radiation source ($\lambda = 1.5405980$ Å), operated at 40 mA, 45 kV, and with a step size of 0.0262606° over a 2θ range from 10° to 70°, in an Eulerian-Cradle geometry. This characterization was performed in a collection of single crystals of each batch, which were cut into tiny fragments and spread in the sample holder to emulate a powder diffraction experiment. This was done with the purpose of obtaining a statistically meaningful characterization of many crystals in each batch. The most intense diffraction peaks for all batches come from the {0 0 1} family of planes, given that the *a*-*b* plane of the crystals tends to align parallel to the sample holder. Few peaks corresponding to different families of planes can still be recognized.

In order to resolve the exact crystal structures of the $x = 1.4\%$ and 7.6% Te-doped samples, single-crystal X-ray diffraction was also measured. The intensities were measured at room temperature, 298 (2) K, using CuKα radiation ($\lambda = 1.54184$ Å), and ω scans in an Agilent SuperNova, Dual, Cu at Zero, Atlas four-circle diffractometer equipped with a CCD plate detector. The collected frames were integrated with the CrysAlis PRO software package (CrysAlisPro 1.171.39.46e, Rigaku Oxford Diffraction, 2018). Data were corrected for the absorption effect using the CrysAlis PRO software package by the empirical absorption correction using spherical harmonics, implemented in the SCALE3 ABSPACK scaling algorithm (CrysAlisPro 1.171.39.46e, Rigaku Oxford Diffraction, 2018). The structures were solved using an iterative algorithm[63] and then completed by a difference Fourier map. The crystal structures were refined using the program SHELXL2018/3[64].

Raman spectroscopy

Raman spectra for crystals of all the compositions studied were taken in a HORIBA Scientific XPLORA Xl041210 Raman spectrometer. The excitation wavelength used for all measurements was 532 nm with a grating of 2400 lines/mm, in the range of 70–1000 cm^{-1}.

Magnetic measurements

Isothermal magnetic hysteresis loops at 300 K and 80 K were measured in a Lakeshore™ 7400 Series vibrating-sample magnetometer (VSM). Cryogenic temperatures were reached through a flow-cryostat operated with liquid nitrogen.

Piezoresponse force microscopy measurements

The piezoelectric effect can be measured through the piezoresponse force microscopy (PFM) technique, which is a variation of the atomic force microscopy (AFM) technique. The piezoresponse is acquired when an AC electrical voltage is applied using a conductive tip in contact with the sample surface. The resulting oscillatory deformation of the sample under the AC voltage is detected through the AFM cantilever deflection. We use two kinds of PFM measurement: Contact resonance (Dual AC Resonance Tracking (DART)) and Switching Spectroscopy (SS-PFM) using a Cypher ES Environmental AFM from Asylum Research, operated at room temperature and in an inert N_2 atmosphere.

In the DART-PFM mode, the cantilever is operated with an AC voltage frequency near the contact resonance frequency, resulting in a driven harmonic oscillator, which enhances the piezoresponse signal, even if it is very small. Similarly, SS-PFM uses a sinusoidal voltage at contact resonance frequency overlapped with square voltages of smaller periods. In ferroelectric materials, it allows the determination of the electromechanical hysteresis loops and their switching parameters, such as coercive and nucleation voltages.

To avoid misunderstandings in piezoresponse amplitude data, arbitrary units (a. u.) are used when piezoresponse amplitude is reported without treatment, whereas picometers (pm) are used when amplitude data is normalized by a single harmonic oscillator (SHO) model[65]. This model provides an accurate way to calculate the real piezoelectric amplitude in the small damping regimen. Moreover, to demonstrate the accuracy of this model and its use in a methodology to obtain the effective piezoelectric constant, d_{33}, in our single crystals, a standard sample of periodically poled lithium niobate (PPLN) was characterized by DART-PFM and SS-PFM using silicon probes (AC240TM-R3). Afterward, the same methodology was used in our doped single crystals (see Supplementary Fig. 8). Experimental spring constants were between 1.71 and 2.95 N/m, and contact-mode resonance frequencies were between 219 and 241 kHz.

Transport properties

The electrical properties of single crystals were measured by a four-probe technique for resistance vs temperature/field measurements and a two-probe technique for current vs voltage measurements using a Keithley 2400 Source Meter. Gold pads were evaporated into the single crystals in order to reduce contact resistance and capacitive effects. Cryogenic temperatures were achieved using an Oxford Instruments liquid helium variable temperature insert cryostat equipped in an IntegraAC Recondensing Helium System.

DFT calculations

First-principles calculations were performed using Density Functional Theory[66] (DFT) as implemented in the Quantum ESPRESSO package[67]. Core electrons were treated within the pseudopotential approximation by means of norm-conserving ultrasoft pseudopotentials. Generalized gradient approximation (GGA) in the parametrization of Perdew-Burke-Ernzerhof (PBE)[68] was chosen for the exchange-correlation (XC) energy functional. Grimme's semiempirical DFT-D3 method[69] was used to include van der Waals interactions between the layers, ignoring three-body terms. The number of plane waves in the basis set corresponds to a kinetic energy cutoff of 50 Ha. Structural optimizations were performed until forces reached a tolerance of 1×10^{-4} a.u.

Starting with the simulation of pure WSe_2, ionic positions and unit cell lattice parameters were optimized. The resulting structural parameters are in good agreement with the measured ones and with previously reported DFT calculations, as can be seen in Supplementary Table 4. Inclusion of both chalcogen vacancies and Te-doping was achieved in a $4 \times 4 \times 1$ supercell, which allowed the simulation of systems with Te-doping and chalcogen vacancy levels similar to the measured single crystals. The effect of vacancies and Te doping on the magnetic behavior was analyzed by performing spin-polarized calculations with and without spin-orbit coupling. For each concentration, a random configuration was selected to perform the calculations. In all cases, a $4 \times 4 \times 3$ Monkhorst-Pack grid[70] was used for sampling the first Brillouin zone.

Berry phase calculations of electric polarization were performed with the implementation found in the ABINIT[71] program using a finer reciprocal space grid of $5 \times 5 \times 3$ points and ONCVPSP[72] pseudopotentials. Hirshfeld charge analysis was performed with the post-processing tool *cut3d* from ABINIT.

Evaluation of activation energy barriers was performed on a $2 \times 2 \times 1$ supercell with one Se vacancy and no Te doping. First Brillouin zone was sampled with a $6 \times 6 \times 3$ grid. This simplification was needed in view of the excessive computational cost of performing NEB calculations on the original $4 \times 4 \times 1$ supercells.

DATA AVAILABILITY

All data related to this work, and the files described in the supplementary information, are publicly available at https://github.com/pgiraldogallo/RoomTmultiferroicityInTMDs-npj2DmatAppl.git.

Received: 16 February 2023; Accepted: 20 July 2023;
Published online: 17 August 2023

REFERENCES

1. Hu, J.-M., Nan, T., Sun, N. X. & Chen, L.-Q. Multiferroic magnetoelectric nanostructures for novel device applications. *MRS Bull.* **40**, 728–735 (2015).
2. Eerenstein, W., Mathur, N. D. & Scott, J. F. Multiferroic and magnetoelectric materials. *Nature* **442**, 759–765 (2006).
3. Béa, H., Gajek, M., Bibes, M. & Barthélémy, A. Spintronics with multiferroics. *J. Phys. Condens. Matter* **20**, 434221 (2008).
4. Scott, J. F. Multiferroic memories. *Nat. Mater.* **6**, 256–257 (2007).
5. Hill, N. A. Why are there so few magnetic ferroelectrics? *J. Phys. Chem. B* **104**, 6694–6709 (2000).
6. Chen, C. et al. Strong *d–d* electron interaction inducing ferromagnetism in Mn-doped $LiNbO_3$. *Thin Solid Films* **520**, 764–768 (2011).
7. Pan, F., Song, C., Liu, X. J., Yang, Y. C. & Zeng, F. Ferromagnetism and possible application in spintronics of transition-metal-doped ZnO films. *Mater. Sci. Eng. R Rep.* **62**, 1–35 (2008).
8. Hanamura, E. & Tanabe, Y. Phase transitions and second-harmonics of ferroelectric and antiferromagnetic $RMnO_3$. *Phase Transit.* **79**, 957–971 (2006).
9. Wang, J. et al. Epitaxial $BiFeO_3$ multiferroic thin film heterostructures. *Science* **299**, 1719–1722 (2003).
10. Ramesh, R. & Spaldin, N. A. Multiferroics: progress and prospects in thin films. *Nat. Mater.* **6**, 21–29 (2007).
11. Tang, X. & Kou, L. Two-dimensional ferroics and multiferroics: platforms for new physics and applications. *J. Phys. Chem. Lett.* **10**, 6634–6649 (2019).
12. Behera, B., Sutar, B. C. & Pradhan, N. R. Recent progress on 2D ferroelectric and multiferroic materials, challenges, and opportunity. *Emergent Mater.* **4**, 847–863 (2021).
13. Gao, Y., Gao, M. & Lu, Y. Two-dimensional multiferroics. *Nanoscale* **13**, 19324–19340 (2021).
14. Song, Q. et al. Evidence for a single-layer van der Waals multiferroic. *Nature* **602**, 601–605 (2022).
15. Zhao, Y. et al. Surface vacancy-induced switchable electric polarization and enhanced ferromagnetism in monolayer metal trihalides. *Nano Lett.* **18**, 2943–2949 (2018).
16. Lyu, H.-Y., Zhang, Z., You, J.-Y., Yan, Q.-B. & Su, G. Two-dimensional intercalating multiferroics with strong magnetoelectric coupling. *J. Phys. Chem. Lett.* **13**, 11405–11412 (2022).

17. Tahir, R., Zahra, S. A., Naeem, U., Akinwande, D. & Rizwan, S. First observation on emergence of strong room-temperature ferroelectricity and multiferroicity in 2D-$Ti_3C_2T_x$ free-standing MXene film. *RSC Adv.* **12**, 24571–24578 (2022).
18. Tahir, R. et al. Multiferroic and ferroelectric phases revealed in 2D $Ti_3C_2T_x$ MXene film for high performance resistive data storage devices. *NPJ 2D Mater. Appl.* **7**, 1–8 (2023).
19. Du, R. et al. Two-dimensional multiferroic material of metallic p-doped SnSe. *Nat. Commun.* **13**, 6130 (2022).
20. Yang, H. et al. Iron-doping induced multiferroic in two-dimensional In_2Se_3. *Sci. China Mater.* **63**, 421–428 (2020).
21. Zhong, T., Li, X., Wu, M. & Liu, J.-M. Room-temperature multiferroicity and diversified magnetoelectric couplings in 2D materials. *Natl Sci. Rev.* **7**, 373–380 (2020).
22. Shao, Z. et al. Multiferroic materials based on transition-metal dichalcogenides: potential platform for reversible control of Dzyaloshinskii-Moriya interaction and skyrmion via electric field. *Phys. Rev. B* **105**, 174404 (2022).
23. Bonilla, M. et al. Strong room-temperature ferromagnetism in VSe_2 monolayers on van der Waals substrates. *Nat. Nanotechnol.* **13**, 289–293 (2018).
24. Sharma, P. et al. A room-temperature ferroelectric semimetal. *Sci. Adv.* **5**, eaax5080 (2019).
25. Tongay, S., Varnoosfaderani, S. S., Appleton, B. R., Wu, J. & Hebard, A. F. Magnetic properties of MoS_2: existence of ferromagnetism. *Appl. Phys. Lett.* **101**, 123105 (2012).
26. Habib, M. et al. Ferromagnetism in CVT grown tungsten diselenide single crystals with nickel doping. *Nanotechnology* **29**, 115701 (2018).
27. Ding, X. et al. Enhanced ferromagnetism in WS_2 via defect engineering. *J. Alloy. Compd.* **772**, 740–744 (2019).
28. Pham, Y. T. H. et al. Tunable ferromagnetism and thermally induced spin flip in vanadium-doped tungsten diselenide monolayers at room temperature. *Adv. Mater.* **32**, 2003607 (2020).
29. Nasr Esfahani, E., Li, T., Huang, B., Xu, X. & Li, J. Piezoelectricity of atomically thin WSe_2 via laterally excited scanning probe microscopy. *Nano Energy* **52**, 117–122 (2018).
30. Wu, W. et al. Piezoelectricity of single-atomic-layer MoS_2 for energy conversion and piezotronics. *Nature* **514**, 470–474 (2014).
31. Weis, R. S. & Gaylord, T. K. Lithium niobate: summary of physical properties and crystal structure. *Appl. Phys. A* **37**, 191–203 (1985).
32. Lee, J.-H. et al. Reliable piezoelectricity in bilayer WSe_2 for piezoelectric nanogenerators. *Adv. Mater.* **29**, 1606667 (2017).
33. Villars, P. *2H-WSe_2 (WSe_2 rt 2H) Crystal Structure*. https://materials.springer.com/isp/crystallographic/docs/sd_0310430 (Springer, 2023).
34. Yu, P. et al. Metal–semiconductor phase-transition in $WSe_{2(1-x)}Te_{2x}$ monolayer. *Adv. Mater.* **29**, 1603991 (2017).
35. Zhang, Z., Zou, X., Crespi, V. H. & Yakobson, B. I. Intrinsic magnetism of grain boundaries in two-dimensional metal dichalcogenides. *ACS Nano* **7**, 10475–10481 (2013).
36. Yun, S. J. et al. Escalating ferromagnetic order via Se-vacancies near vanadium in WSe_2 monolayers. *Adv. Mater.* **34**, 2106551 (2022).
37. Han, S. W. et al. Controlling ferromagnetic easy axis in a layered MoS_2 single crystal. *Phys. Rev. Lett.* **110**, 247201 (2013).
38. Tao, L. et al. Experimental and theoretical evidence for the ferromagnetic edge in WSe_2 nanosheets. *Nanoscale* **9**, 4898–4906 (2017).
39. Zhou, J. et al. Large-area and high-quality 2D transition metal telluride. *Adv. Mater.* **29**, 1603471 (2017).
40. Wang, Z. et al. 2H/1T′ phase $WS_{2(1-x)}Te_{2x}$ alloys grown by chemical vapor deposition with tunable band structures. *Appl. Surf. Sci.* **504**, 144371 (2020).
41. Cho, S. et al. Phase patterning for ohmic homojunction contact in $MoTe_2$. *Science* **349**, 625–628 (2015).
42. Ding, W. et al. Highly ambient-stable 1T-MoS_2 and 1T-WS_2 by hydrothermal synthesis under high magnetic fields. *ACS Nano* **13**, 1694–1702 (2019).
43. Lin, J. et al. Anisotropic ordering in 1T′ molybdenum and tungsten ditelluride layers alloyed with sulfur and selenium. *ACS Nano* **12**, 894–901 (2018).
44. Duerloo, K.-A. N., Ong, M. T. & Reed, E. J. Intrinsic piezoelectricity in two-dimensional materials. *J. Phys. Chem. Lett.* **3**, 2871–2876 (2012).
45. Rogée, L. et al. Ferroelectricity in untwisted heterobilayers of transition metal dichalcogenides. *Science* **376**, 973–978 (2022).
46. Rawat, A. et al. Nanoscale interfaces of janus monolayers of transition metal dichalcogenides for 2D photovoltaic and piezoelectric applications. *J. Phys. Chem. C* **124**, 10385–10397 (2020).
47. Chen, Y. et al. 2D transition metal dichalcogenide with increased entropy for piezoelectric electronics. *Adv. Mater.* **34**, 2201630 (2022).
48. Hong, S. et al. Principle of ferroelectric domain imaging using atomic force microscope. *J. Appl. Phys.* **89**, 1377–1386 (2001).
49. Covaci, C. & Gontean, A. Piezoelectric energy harvesting solutions: a review. *Sensors* **20**, 3512 (2020).
50. Briscoe, J. & Dunn, S. *Nanostructured Piezoelectric Energy Harvesters*. https://www.springerprofessional.de/en/nanostructured-piezoelectric-energy-harvesters/2223256 (Springer, 2014).
51. Yan, F., Xing, G. Z. & Li, L. Low temperature dependent ferroelectric resistive switching in epitaxial $BiFeO_3$ films. *Appl. Phys. Lett.* **104**, 132904 (2014).
52. Sawa, A. Resistive switching in transition metal oxides. *Mater. Today* **11**, 28–36 (2008).
53. Resta, R. Macroscopic electric polarization as a geometric quantum phase. *EPL* **22**, 133 (1993).
54. Hirshfeld, F. L. Bonded-atom fragments for describing molecular charge densities. *Theor. Chim. Acta* **44**, 129–138 (1977).
55. Wu, M. & Li, J. Sliding ferroelectricity in 2D van der Waals materials: related physics and future opportunities. *Proc. Natl Acad. Sci. USA* **118**, e2115703118 (2021).
56. Trevethan, T., Latham, C. D., Heggie, M. I., Rayson, M. J. & Briddon, P. R. Interlayer vacancy diffusion and coalescence in graphite. *Phys. Rev. B* **90**, 174108 (2014).
57. Henkelman, G. & Jónsson, H. Improved tangent estimate in the nudged elastic band method for finding minimum energy paths and saddle points. *J. Chem. Phys.* **113**, 9978–9985 (2000).
58. Li, L. & Wu, M. Binary compound bilayer and multilayer with vertical polarizations: two-dimensional ferroelectrics, multiferroics, and nanogenerators. *ACS Nano* **11**, 6382–6388 (2017).
59. Shidpour, R. & Manteghian, M. A density functional study of strong local magnetism creation on MoS_2 nanoribbon by sulfur vacancy. *Nanoscale* **2**, 1429–1435 (2010).
60. Matsubara, M. et al. Magnetoelectric domain control in multiferroic $TbMnO_3$. *Science* **348**, 1112–1115 (2015).
61. Wu, H. et al. Ising magnetism and ferroelectricity in Ca_3CoMnO_6. *Phys. Rev. Lett.* **102**, 026404 (2009).
62. Fei, Z. et al. Ferroelectric switching of a two-dimensional metal. *Nature* **560**, 336–339 (2018).
63. Palatinus, L. & Chapuis, G. SUPERFLIP—a computer program for the solution of crystal structures by charge flipping in arbitrary dimensions. *J. Appl. Cryst.* **40**, 786–790 (2007).
64. Sheldrick, G. M. Crystal structure refinement with SHELXL. *Acta Cryst. C* **71**, 3–8 (2015).
65. García, R. & Pérez, R. Dynamic atomic force microscopy methods. *Surf. Sci. Rep.* **47**, 197–301 (2002).
66. Kohn, W. & Sham, L. J. Self-consistent equations including exchange and correlation effects. *Phys. Rev.* **140**, A1133–A1138 (1965).
67. Giannozzi, P. et al. QUANTUM ESPRESSO: a modular and open-source software project for quantum simulations of materials. *J. Phys. Condens. Matter* **21**, 395502 (2009).
68. Perdew, J. P., Burke, K. & Ernzerhof, M. Generalized gradient approximation made simple. *Phys. Rev. Lett.* **77**, 3865–3868 (1996).
69. Grimme, S., Antony, J., Ehrlich, S. & Krieg, H. A consistent and accurate ab initio parametrization of density functional dispersion correction (DFT-D) for the 94 elements H-Pu. *J. Chem. Phys.* **132**, 154104 (2010).
70. Monkhorst, H. J. & Pack, J. D. Special points for Brillouin-zone integrations. *Phys. Rev. B* **13**, 5188–5192 (1976).
71. Gonze, X. et al. The Abinitproject: impact, environment and recent developments. *Comput. Phys. Commun.* **248**, 107042 (2020).
72. Hamann, D. R. Optimized norm-conserving Vanderbilt pseudopotentials. *Phys. Rev. B* **88**, 085117 (2013).

ACKNOWLEDGEMENTS

The authors thank A. Castellanos-Gómez and C. Munuera for enlightening discussions, and Daniel Dorado and Duvan Martínez for their contribution to IV curves measurements. All authors acknowledge the financial support provided by the Vice Presidency for Research & Creation publication fund at the Universidad de los Andes. G.C.-C., K.V.-B., J.P., O.H., C.E., W.L.P., J.A.G. and P.G.-G. thank the financial support of the Ministerio de Ciencia, Tecnología e Innovación de Colombia, through Grant No. 122585271058. C.E. and W.L.P. acknowledge computational resources from Granado-HPC, Universidad del Norte. P.G.-G. and K.V.-B. thank the support of the School of Sciences and the Vice Presidency of Research Creation at Universidad de Los Andes. P.G.-G., G.C.-C. and K.V.-B. thank the financial support of Fundación para la promoción de la investigación y la tecnología (FPIT), of Banco de la República de Colombia, Project number 4.687. J.A.G., J.P. and O.H. thank the support of Clúster de Investigación en Ciencias y Tecnologías Convergentes NBIC, Universidad Central. P.G.-G. and D.S.-V. thank the support of the Consejo Superior de Investigaciones Científicas (CSIC) of Spain through the i-COOP+2020 project, #COOPA20460.

AUTHOR CONTRIBUTIONS

G.C.-C., K.V.-B., H.R.-P. and P.G.-G. performed the materials synthesis. G.C.-C., K.V.-B. and M.A.M. performed the structural and compositional characterization. G.C.-C., K.V.-B., and J.P. performed the magnetic and PFM measurements. G.C.-C., K.V.-B. and D.S.-V. performed transport measurements. G.C.-C., K.V.-B. and P.G.-G. led the experimental data analysis. C.E. and W.L.-P. performed the DFT calculations. P.G.-G., J.A.G., C.E., W.L.-P. and O.H. conceived the project and secured funds. All authors participated in the discussion of the data and manuscript writing.

COMPETING INTERESTS

The authors declare no competing interests.

ADDITIONAL INFORMATION

Supplementary information The online version contains supplementary material available at https://doi.org/10.1038/s41699-023-00416-x.

Correspondence and requests for materials should be addressed to P. Giraldo-Gallo.